Solution Structure and Backbone Dynamics of the Cu(I) and Apo Forms of the Second Metal-Binding Domain of the Menkes Protein ATP7A†

Lucia Banci,‡,§ Ivano Bertini,*,‡,§ Rebecca Del Conte,‡,§ Mariapina D'Onofrio,‡ and Antonio Rosato‡,§

Magnetic Resonance Center, University of Florence, Via L. Sacconi 6, 50019 Sesto Fiorentino, Italy, and Department of Chemistry, University of Florence, Via della Lastruccia 3, 50019 Sesto Fiorentino, Italy

Received November 14, 2003; Revised Manuscript Received January 29, 2004

ABSTRACT: The second domain of the human Menkes protein (MNK2), formed by 72 residues, has been expressed in *Escherichia coli*, and its structure has been determined by NMR in both the apo and copper-loaded forms. The structures, obtained with ^{13}C- and ^{15}N-labeled samples, are of high quality with backbone rmsd values of 0.51 and 0.41 Å and CYANA target functions of 0.39 and 0.38 Å^2, respectively. The loop involved in copper binding is part of a hydrophobic patch, which is maintained in both forms. Conformational mobility is observed in the apo form in the same loop. A comparison with metallochaperones and soluble domains of P-type ATPases allows us to relate the primary structure to the occurrence of structural rearrangements upon copper binding.

Copper, an essential trace metal, is utilized as a cofactor in a variety of redox and hydrolytic proteins. In eukaryotes, copper-dependent metalloenzymes are found in multiple cellular locations (*1*). Excess copper, however, is highly toxic to most organisms (*1*, *2*). Accordingly, a complex machinery of proteins that bind the metal ion strictly controls the uptake, transport, sequestration, and efflux of copper *in vivo* (*3*−*5*). In particular, so-called metallochaperones deliver copper to specific intracellular targets, acting like enzymes to lower the activation barrier for transfer of copper to their specific partners (*6*), thereby circumventing the significant thermodynamic overcapacity for copper chelation of the cytoplasm (*7*).

In humans, there are three key proteins in the copper transport pathway that are relevant to this work. HAH1 (that is, human Atx1, also known as Atox1) is a soluble metallochaperone (*8*, *9*) which is capable of delivering copper(I) to both the Menkes and Wilson disease proteins (ATP7A and ATP7B, respectively) (*3*−*5*). The latter two proteins are membrane-bound P-type ATPases which translocate copper in the trans-Golgi network or across the plasma membrane (*3*−*5*), depending on the environmental conditions (*10*). In fact, both proteins experience copper-regulated trafficking between the Golgi and plasma membranes (*10*). ATP7A and ATP7B possess a long N-terminal cytosolic tail containing six putative metal-binding domains whose sequences are significantly similar to one another as well as to that of HAH1. Homologues of HAH1, ATP7A, and ATP7B are found in a number of prokaryotic and eukaryotic organisms; however, it is noteworthy that the genome of some organisms may encode only one of the two partners (*11*). The number of metal-binding domains in ATP7A and ATP7B homologues is variable, ranging from one to six, with proteins from higher eukaryotic organisms, e.g., mammals, having a higher number of such domains than prokaryotic (typically one or two) or yeast (two) homologues (*11*, *12*).

X-ray crystallography and NMR[1] spectroscopy have provided structures of various metal-binding domains in different metalation states for both metallochaperones and the partner ATPases (for reviews, see refs *13* and *14*). In some cases, the dynamic properties of the apo- and/or holoproteins have been directly probed by NMR in solution (*14*). The interaction between the two partners has been experimentally characterized at the atomic level through NMR studies on the yeast and *Bacillus subtilis* systems (*15*, *16*), and found to be in agreement with previous suggestions based on the X-ray structure of nonphysiological self-adducts (*17*).

As far as ATP7A is concerned, the structure of the fourth domain (MNK4) has been determined in solution in the apo and Ag(I) forms, but not in the physiologically relevant copper(I) form (*18*). A structure of the apo form of the second domain (MNK2) just became available, but again there is no structure for the copper(I) form (*19*). No dynamic information is available for any of the ATP7A metal-binding domains. An extensive characterization of the human ATPase

† This work was supported by MIUR-COFIN 2001, Ente Cassa di Risparmio di Firenze, and the European Commission (Contract QLG2-CT-2002-00988).

* To whom correspondence should be addressed: Magnetic Resonance Center, University of Florence, Via L. Sacconi, 6, 50019 Sesto Fiorentino, Italy. Fax: +39 055 4574271. Telephone: +39 055 4574272. E-mail: bertini@cerm.unifi.it.

‡ Magnetic Resonance Center.

§ Department of Chemistry.

[1] Abbreviations: NMR, nuclear magnetic resonance; REM, restrained energy minimization; rmsd, root-mean-square deviation; TOCSY, total correlation spectroscopy; NOE, nuclear Overhauser effect; NOESY, nuclear Overhauser effect spectroscopy; HMQC, heteronuclear multiple-quantum coherence; HSQC, heteronuclear single-quantum coherence; INEPT, insensitive nuclei enhanced by polarization transfer; WATERGATE, water suppression by gradient-tailored excitation; TPPI, time-proportional phase incrementation; WEFT, water-eliminated Fourier transform; MNK2, second metal-binding domain of the human Menkes protein (ATP7A); MNK4, fourth metal-binding domain of the human Menkes protein (ATP7A).

10.1021/bi036042s CCC: $27.50
Published on Web 03/03/2004

metal-binding domains is desirable not only because of the greater interest for direct investigation of human proteins instead of their homologues (e.g., yeast) but also because the specific reasons higher organisms have as many as six metal-binding domains are still unclear. More importantly, a detailed characterization of the process of copper transfer would contribute to the understanding of the diseases caused by its malfunctioning. Available studies on ATP7A or ATP7B trying to address this matter indicate some functional differentiation between the first four (counting from the N-terminus) and the last two domains, and suggest that the last two domains are sufficient for function (*20*−*22*). In addition, the mechanism of transfer of copper(I) from HAH1 to either human ATPase has also not been completely elucidated. In this respect, it is noteworthy that homology modeling of the ATP7A metal-binding domains shows significant variations among the various domains in the electrostatic surface implicated in partner recognition, potentially making it possible for them to interact with one another (*11*).

In this paper, a structural and dynamic characterization of MNK2 is reported for both the apo and copper(I) forms. The features of this domain are compared with those of the other domains and homologous proteins.

MATERIALS AND METHODS

Protein Expression and Purification. The DNA sequence encoding MNK2, corresponding to amino acids 169−240 of ATP7A, was amplified via PCR and cloned into pET20b+ (Novagen) between the *Nde*I and *Xho*I restriction sites so that the expressed protein additionally contains a recognition site for protease factor Xa and a His_6 tag at the C-terminal end. After cleavage of the tag, four amino acids from the restriction site are left at the C-terminus of the protein. In the following, residues will be numbered from 1 to 76, rather than starting from 169, for the sake of simplicity.

The plasmid (pMP1) described above was transformed into *Escherichia coli* strain BL21(DE3)pLysS for protein expression. Cells were grown at 37 °C in LB, ^{15}N-Silantes Medium, or ^{15}N,^{13}C-Silantes Media to produce unlabeled, ^{15}N-labeled, or ^{15}N- and ^{13}C-labeled samples, respectively. Ampicillin (100 μg/mL) and chloramphenicol (34 μg/mL) were added to the culture medium. Protein expression was induced using 1 mM isopropyl 1-thio-β-D-galactopyranoside when the A_{600} was ∼0.6, and the cells were harvested 4 h thereafter.

All protein purification steps were carried out in an N_2 atmosphere chamber by affinity chromatography with a HiTrap 5 mL affinity column (Amersham Pharmacia Biotech) previously charged with Zn^{2+}. After purification, the His_6 tag was cut by overnight incubation with factor Xa (40 μg of enzyme per 20 mg of recombinant protein). The protein without the His_6 tag was purified by passing the solution again through the HiTrap column charged with Zn^{2+}, under conditions where the uncut protein would stick to the column.

The recombinant protein finally produced was characterized by mass spectroscopy, circular dichroism, and atomic absorption.

NMR Sample Preparation. Apoprotein samples were reduced with excess dithiothreitol (DTT) and washed with 100 mM sodium phosphate buffer at pH 7.0. The final molar ratio of DTT to protein was typically 2−5. Copper(I)-containing protein samples were prepared as previously described (*6*). Sample preparation was carried out in an N_2 atmosphere chamber, and the NMR tubes were sealed before they were removed from the chamber. The final protein concentration in all samples was ∼1 mM. NMR samples also contained 10% (v/v) ^2H_2O for an NMR spectrometer lock.

NMR Spectral Analysis. All two- and three-dimensional (2D and 3D, respectively) spectra were collected at 298 K, unless otherwise indicated, processed using the standard Bruker software (XWINNMR), and analyzed using XEASY (*23*). Tables S1 and S2 of the Supporting Information summarize the experiments performed on apo- and holo-MNK2, respectively.

The peaks used for structure calculations were integrated in the 2D NOESY map, as well as in the 3D ^{15}N and ^{13}C NOESY-HSQC spectra. Intensities of dipolar connectivities were converted into upper distance limits using CALIBA (*24*). Each peak list was calibrated independently. Stereospecific assignments of diastereotopic protons were obtained using the HNHB experiment (*25*) and the program GLOMSA (*24*).

$^3J_{HNH\alpha}$ coupling constants were used to derive constraints for the backbone ϕ dihedral angle by means of the appropriate Karplus curve (*26*). ϕ angle constraints were further obtained from the ratio between intraresidue and sequential HN−Hα NOESY cross-peak intensities (*27*) and the secondary structure indicated by the chemical shift index (CSI) (*28*), both of which were also used to extract ψ torsion angles.

Structure Calculations. Structure calculations were performed using CYANA (*29*). The CANDID module of CYANA (*30*) was exploited for automated assignment of the NOESY cross-peaks, followed by a manual check prior to the final calculations. Two hundred random conformers were annealed in 10 000 steps using the constraints described above. The 30 conformers with the lowest target function constituted the final family.

The copper ion was included in the calculations following a procedure already reported, which does not impose any fixed orientation of the ligands with respect to the copper [e.g., with respect to the Sγ−Cu(I)−Sγ angle] (*31*). Restrained energy minimization (REM) was performed for each member of the final family of conformers using AMBER 6 (*32*). The force field parameters for the copper(I) ion were taken as in similar systems (*33*). In particular, no constraint on the Sγ(Cys14)−Cu−Sγ(Cys17) angle was used. Force constants of 50 kcal mol^{-1} Å^{-2} and 32 kcal mol^{-1} rad^{-2} were used for NOE and torsion angle constraints, respectively.

The quality of the structure was evaluated in terms of deviations from ideal bond lengths and bond angles and through Ramachandran plots obtained using PROCHECK (*34*) and PROCHECK-NMR (*35*). Structure calculations and analysis were performed on a cluster of Linux personal computers. The two final structures and the constraints used for calculations have been deposited with the Protein Data Bank (entry 1S6O for apo-MNK2 and entry 1S6U for holo-MNK2).

NMR Mobility Data Acquisition and Analysis. NMR experiments for determination of ^{15}N longitudinal and transverse relaxation rates (*36*) and ^{1}H−^{15}N NOE (*37*) were recorded at 298 K at 600 MHz. R_1 and R_2 relaxation rates were obtained by fitting the cross-peak volumes (I), measured

as a function of the relaxation delay, to a single-exponential decay by using the Levenberg−Marquardt algorithm (*38*), as described in the literature (*39*). Uncertainties had been evaluated by using a Monte Carlo approach (*39*). Heteronuclear NOE values were calculated as the ratio of peak volumes in spectra recorded with and without saturation.

RESULTS

Protein Characterization. Mass spectroscopy confirmed the expected mass for the MNK2 construct described herein (experimental value of 8444 Da vs an expected value of 8447 Da), including the extra four amino acids at the protein C-terminus, which are left after cleavage of the protein with protease Factor Xa. Analytical data indicate binding of a single copper(I) ion per molecule (experimental ratio by atomic absorption of 1.1), with CD spectroscopy showing good folding in both the apo and copper(I) forms.

At variance with previous reports for a larger MNK2 construct (*19*), apo- and holo-MNK2 samples are stable at ~1 mM for several weeks, allowing us to record ^{15}N,^{13}C 3D heteronuclear spectra (Tables S1 and S2 of the Supporting Information). Both apo- and holo-MNK2 exhibit well-resolved and well-dispersed ^{1}H−^{15}N HSQC spectra, indicative of well-folded proteins. The signal line widths (then confirmed by direct ^{15}N relaxation measurements) are indicative of a monomeric state for the protein in solution.

Assignment of NMR Spectra and Structural Calculations. Backbone assignments were obtained using standard strategies based on triple-resonance experiments (*40*). For both apo- and holo-MNK2, all residues were assigned. In ^{15}N HSQC spectra, it was not possible to detect the resonances of the backbone amide moieties of Gly1 and His15 in both protein forms, and of Ser16 in apo-MNK2. While the nondetectability of Gly1 is most likely due to rapid proton exchange with the solvent, the lack of signals from His15 and Ser16 could originate from conformational exchange processes, more prominent in the apo than in the holo form. This matter is directly addressed by ^{15}N relaxation measurements (see later). Overall, the percentages of backbone assignments achieved are as follows (excluding residue 1). For apo-MNK2, 95% of ^{15}N, 100% of ^{13}Cα, 97% of HN, and 100% of Hα resonances were assigned, and for holo-MNK2, 96% of ^{15}N, 100% of ^{13}Cα, 99% of HN, and 100% of Hα resonances were assigned. The assignment of the side chain resonances was performed through the analysis of 3D H(C)CH-TOCSY and CC(CO)HN spectra together with ^{15}N NOESY-HSQC and ^{13}C NOESY-HSQC spectra. In this way, more than 90% of the total proton and ^{13}C resonances were assigned. Resonance assignments are reported as Supporting Information. Variations in the ^{15}N and ^{13}Cα chemical shifts between apo- and holo-MNK2 are shown in Figure 1; chemical shift variation plots for the HN and Hα protons show an analogous pattern, on a somewhat reduced scale. It appears that all major chemical shift variations occurring consistently for the two heteronuclei are located between residue 12 and residue 19, i.e., from two residues before the first copper(I) ligand (Cys14) up to two residues after the second copper(I) ligand (Cys17). The data in Figure 1 are consistent with the data for the HN chemical shift variations recently reported for the titration of a different construct of MNK2 (*19*). A direct comparison is however not feasible because of different buffer conditions.

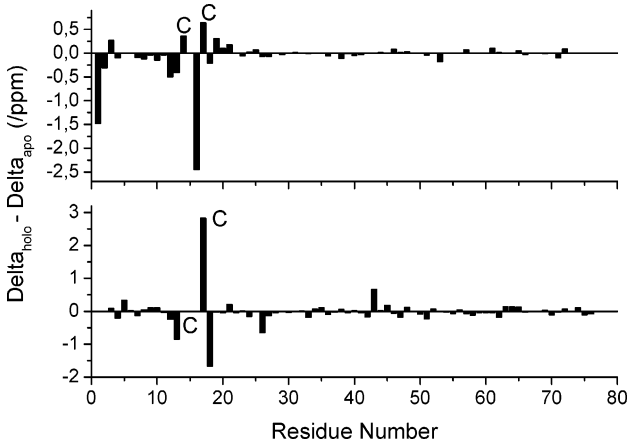

FIGURE 1: Chemical shift variations for ^{13}Cα (top) and backbone ^{15}N (bottom) nuclei of MNK2 upon copper(I) binding. Cysteines are labeled.

Solution Structures. For structure calculations of apo- and holo-MNK2, 1237 and 1243 meaningful upper distance limits, respectively, were used. In addition, 32 ϕ and 32 ψ torsion angles were constrained in each protein form. A breakdown of the constraints that were used is given in Tables 1 and 2 for apo- and holo-MNK2, respectively. The constraints used for all calculations are given in the Supporting Information.

The final (after REM refinement) apo-MNK2 family has an average total target function of 0.39 ± 0.02 Å^2 (CYANA units), while the corresponding value for the holo-MK2 family is 0.38 ± 0.03 Å^2. The average backbone rmsd values (over residues 3−74) for the apo- and holo-MNK2 structures are 0.51 ± 0.06 and 0.41 ± 0.10 Å, respectively; the all heavy atom rmsd values instead are 1.08 ± 0.12 and 0.92 ± 0.12 Å, respectively. Tables 1 and 2 report some statistics on constraint violations in the final families together with selected quality parameters from a PROCHECK-NMR (*35*) analysis. These data indicate that the solution structures obtained for both apo- and holo-MNK2 are of good quality.

Figure 2 shows a comparison of the structures of apo- and holo-MNK2, highlighting the metal site structure in the latter. Both structures adopt the ferredoxin-like $\beta\alpha\beta\beta\alpha\beta$ fold. The rmsd between the backbone atoms for the mean structures of the two families of conformers, excluding the metal-binding loop region and the poorly defined C-terminal tail, is 1.1 Å. Table 3 shows the elements of regular secondary structure detected by PROCHECK-NMR in the two structures.

The sulfur−copper−sulfur angle in holo-MNK2 is found to be 140 ± 40°. This value is closer to 180° than what was observed for the corresponding yeast homologue, Ccc2 (119 ± 29°), even though not significantly so from a statistical point of view, but still indicative of deviation from ideal linear diagonal coordination. To assess the conformation of the copper(I) site, calculations were also performed without inclusion of links with the copper ion. In the majority of the members of this family, the conformation of Cys14 was quite close to that observed when coordination to the copper ion was imposed, and the conformation of Cys17 was essentially identical. These results thus indicate that the cysteine conformation in copper(I)-bound MNK2 is defined well by the experimental structural constraints.

Table 1: Summary of NMR Constraints Used for Structure Calculation, Restraint Violations, Structural Statistics, and Energetics for the Restrained Energy-Minimized Solution Structure of Apo-MNK2

		REM		⟨REM⟩	
	no.	average no. of violations per conformer	rms violation per restraint	no. of violations	rms violation per restraint
structural constraints					
meaningful NOESY	1237	47 ± 3	0.017 ± 0.001	48	0.017
intraresidue	435	24.9 ± 2.7	0.021 ± 0.002	29	0.021
sequential	328	9.2 ± 1.8	0.014 ± 0.001	8	0.015
medium-range	205	6.5 ± 1.5	0.013 ± 0.002	5	0.012
long-range	269	6.6 ± 1.8	0.014 ± 0.002	6	0.015
Φ	32	1.40 ± 0.95	0.9 ± 0.5	2	2.3
Ψ	32	0.90 ± 0.55	0.8 ± 0.5	0	0.0
no. of violations between 0.1 and 0.3 Å		10.9 ± 2.5		13	
no. of violations larger than 0.3 Å		0.00 ± 0.00		0.0	
largest distance violation (Å)		0.22			0.15
largest Φ violation (deg)		8.0			12.8
largest Ψ violation (deg)		7.9			−
energetics					
total target function (Å^2)		0.39 ± 0.03			0.43
Amber average energy (kJ/mol)		−3300 ± 250			−3272
structure analysis					
completeness of ^{13}C backbone assignment (%)			100		
completeness of ^{15}N backbone assignment (%)			95		
completeness of ^{1}H backbone assignment (%)			98		
no. of meaningful structural constraints per residue			17.1		
residues in most favored regions (%)[a]		74.2			74.2
residues in allowed regions (%)[a]		22.4			22.7
residues in generously allowed regions (%)[a]		1.9			1.5
residues in disallowed regions (%)[a]		1.5			1.5
overall *G*-factor[b]		−1.01			−0.96

[a] As defined by the Ramachandran plot. [b] As defined in the program PROCHECK (*34*).

Table 2: Summary of NMR Constraints Used for Structure Calculation, Restraint Violations, Structural Statistics, and Energetics for the Restrained Energy-Minimized Solution Structure of Copper(I)-Bound MNK2

		REM		⟨REM⟩	
	no.	average no. of violations per conformer	rms violation per restraint	no. of violations	rms violation per restraint
structural constraints					
meaningful NOESY	1243	48 ± 4	0.016 ± 0.001	48	0.016
intraresidue	431	27.5 ± 3.0	0.021 ± 0.001	28	0.021
sequential	278	8.5 ± 1.7	0.012 ± 0.001	8	0.011
medium-range	240	6.1 ± 1.4	0.015 ± 0.001	6	0.015
long-range	294	6.1 ± 1.5	0.014 ± 0.002	6	0.011
Φ	32	0.63 ± 0.71	0.4 ± 0.4	1	0.7
Ψ	32	0.60 ± 0.49	0.5 ± 0.4	1	0.6
no. of violations between 0.1 and 0.3 Å		9.2 ± 1.7		8	
no. of violations larger than 0.3 Å		0.00 ± 0.00		0.0	
largest distance violation (Å)		0.22			0.16
largest Φ violation (deg)		4.5			3.9
largest Ψ violation (deg)		6.4			3.6
energetics					
total target function (Å^2)		0.38 ± 0.03			0.35
Amber average energy (kJ/mol)		−3500 ± 270			−3511
structure analysis					
completeness of ^{13}C backbone assignment (%)			100		
completeness of ^{15}N backbone assignment (%)			95		
completeness of ^{1}H backbone assignment (%)			98		
no. of meaningful structural constraints per residue			17.2		
residues in most favored regions (%)[a]		79.6			83.3
residues in allowed regions (%)[a]		17.6			15.2
residues in generously allowed regions (%)[a]		2.4			1.5
residues in disallowed regions (%)[a]		0.3			0.0
overall *G*-factor[b]		−0.84			−0.80

[a] As defined by the Ramachandran plot. [b] As defined in the program PROCHECK (*34*).

Protein Dynamics in Solution. The dynamic properties of apo- and holo-MNK2 have been directly sampled through ^{15}N relaxation measurements (*41*). Both protein forms were found to be monomeric in solution, as also observed for Ccc2 (*16*). ^{15}N relaxation data indicate that MNK2 in both forms is quite uniformly rigid on the nanosecond to picosecond time scale, with the exception of the N- and C-terminal tails; the additional amino acids resulting from the recognition site

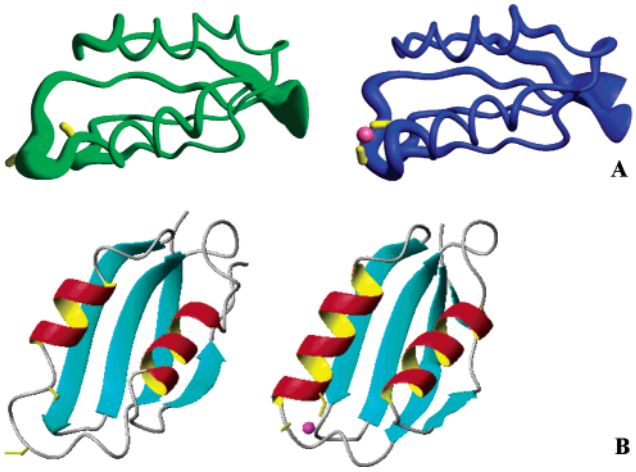

FIGURE 2: Comparison of the solution structures of apo- (left) and copper(I)-bound MNK2 (right). In panel A, the two families are compared using a representation as a tube with variable radius, proportional to the local backbone rmsd. In panel B, the two energy-minimized average structures are compared, using a ribbon representation. This figure was prepared with MOLMOL (*48*). The side chains of Cys14 and Cys17 are shown in yellow; the copper(I) ion is shown as a pink sphere.

Table 3: Elements of Regular Secondary Structure in the Apo-MNK2 and Copper(I)-Bound MNK2 Solution Structures

secondary structure element	residues involved in apo-MNK2	residues involved in copper(I)-bound MNK2
β_1	3−8	3−9
α_1	19−25	15−26
β_2	31−37	31−37
β_3	42−47	42−47
α_2	55−64	54−64
β_4	69−72	69−72

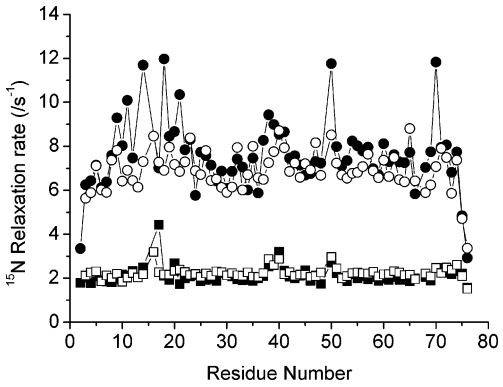

FIGURE 3: ^{15}N R_1 (squares) and R_2 (circles) relaxation rates for apo-MNK2 (filled symbols) and holo-MNK2 (empty symbols).

of protease factor Xa are in fact the most flexible region of the protein, as shown both by ^{15}N R_1 and R_2 relaxation rates (Figure 3) and ^{1}H−^{15}N NOE values (not shown). Apo-MNK2 features conformational averaging involving several residues in the stretch of residues 9−21, i.e., involving the copper(I)-binding loop, which is not observed for holo-MNK2 (Figure 3).

DISCUSSION

As expected, in solution MNK2 adopts the classical $\beta\alpha\beta\beta\alpha\beta$ ferredoxin fold regardless of the presence of the metal ion. As observed for other proteins of this class (*13*, *14*), in copper(I)-bound MNK2 the copper ion is close to the protein surface and exposed to the solvent. The coordinates for the recently published (*19*) NMR structure of apo-MNK2 were not available at the time this work was submitted. All the main features of the apo-MNK2 structure presented here appear, as expected, to be in agreement with those previously reported, notwithstanding the different boundaries used to define and express the domain (*19*). Chemical shift variations observed between apo- and holo-MNK2 indicate that perturbations due to copper(I) binding affect mainly the Cys-containing loop (loop 1) and the N-terminal region of the first α-helix (*19*). Indeed, the superposition of the two structures highlights that this is the region where structural rearrangement occurs upon metal binding, while the remainder of the polypeptide chain experiences negligible structural variations (Figure 2B). For the two copper(I)-binding cysteines, the largest conformational rearrangement is observed for Cys14, while the rearrangement for Cys17 is small. However, it is to be noted that the conformation of Cys14 in the apo-MNK2 family of conformers is not very precisely defined. An additional structural variation that can be detected is in the length of helix α_1, which is longer in the copper(I) form (Figure 2 and Table 3). The reciprocal orientation of the two α-helices as well as their orientation with respect to the β-sheet also experiences a small variation upon copper(I) loading. Analogous variations have been reported for the yeast metallochaperone, Atx1 (*42*), but not for the yeast ATP7A homologue, Ccc2 (*31*).

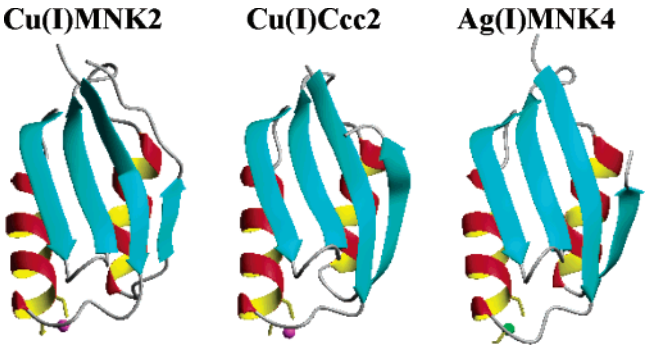

FIGURE 4: Ribbon representations of the structures of (from left to right) copper(I)-bound MNK2, copper(I)-bound Ccc2 (*31*), and silver(I)-bound MNK4 (*18*). The side chains of the metal-binding cysteines are shown in yellow; the metal ions are shown as pink [copper(I)] or green [silver(I)] spheres.

The structure of MNK2 is similar both to that of the first metal-binding domain of the homologous yeast protein Ccc2 (*31*) and to that of MNK4 **(**Figure 4**)**. With respect to these two systems, the most interesting difference is probably that the system presented here shows variations in the structure of the metal-binding loop in the apo- and holoprotein larger than those observed for the other two proteins. This rearrangement is also accompanied by variations in protein dynamics, with the apoprotein featuring conformational exchange processes that are absent in holo-MNK2. Such processes were also indirectly observed in ref *19*. Instead, in the case of Ccc2, protein dynamics were also largely unaffected by copper(I) binding (*16*).

In MNK2, MNK4, and Ccc2, residues Met12, Cys17 (loop 1, i.e., the copper-binding loop), Leu38 (loop 3), and Phe66 (loop 5) form a single compact core, through a network of

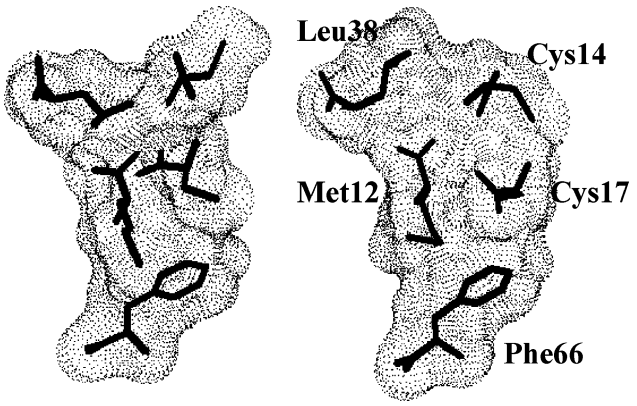

FIGURE 5: Comparison of the van der Waals interactions involving loop I (Met12, Cys14, and Cys17), loop III (Leu38), and loop V (Phe66) in apo-MNK2 (left) and copper(I)-bound MNK2 (right).

hydrophobic contacts, which is present in both the apo- and holoproteins despite some conformational rearrangement of the side chains (Figure 5). This finding is supported by the similarity of NOE patterns observed for the two protein forms, and is in contrast with the structural rearrangement of Phe66 previously proposed on the basis of the analysis of HN chemical shift variations upon copper binding to apo-MNK2 (*19*). On the same basis, a structural rearrangement was proposed also for Gly29 and Gly32, which is not observed here. Met12 is conserved in all eukaryotic ATPases; Leu38 is conserved in all mammal ATPases and replaced with another hydrophobic residue in only 6% of the eukaryotic ATPase domains, while Phe66 is always replaced with a Pro in the third domain of mammal ATPases (in both Menkes and Wilson protein homologues) (*11*). The variation in the side chain contacts and solvent accessibility caused by the substitution of Phe66 with Pro should have an effect on the stability of both the protein and metal site structures, suggesting that the strict conservation of the substitution pattern for residue 66 in mammals is functionally relevant. The copper(I) binding properties of a Phe66 to Ile mutant of MNK2 are, however, essentially identical to those of the wild-type protein (*19*). In both domains of the *Bacillus subtilis* homologue of ATP7A, CopA, copper(I) binding induces a rearrangement of the hydrophobic cluster discussed above (*43*). The large majority of bacterial ATP7A homologues feature a Tyr residue in position 66.

In the partner metallochaperones, there are two major differences with respect to the ATPases (*44*). (i) The four above-mentioned residues never form a single core, but only form pairwise contacts. (ii) Structural rearrangements upon copper(I) binding induce a reorganization of the contacts between the apo- and holoproteins, which affects the solvent accessibility of the copper site and thus may be relevant for the transfer of copper from the chaperone to the partner ATPase. A Tyr residue is found in position 66 in all bacterial metallochaperones, while it is replaced with a Lys in eukaryotic proteins (*11*). Given also the results observed for the *B. subtilis* ATP7A homologue, it is tempting to propose that the presence of Phe or Tyr in position 66 correlates with the absence or presence of structural rearrangements induced by copper(I) binding. In yeast Atx1, a similar structural rearrangement is also observed, which may suggest that Lys is also able to induce a structural rearrangement (*44*).

MNK2 and MNK4 have similar electrostatic charge distributions at the surface (*11*); in particular, in the exposed patch which is directly involved in partner recognition as found in the adduct between Ccc2a and Atx1 (i.e., the two physiological partners in yeast), MNK2 and MNK4 share significant analogies in the pattern of positive, negative, and hydrophobic charges at the surface. Interestingly, this pattern is closer to that of yeast Atx1 than to that of Ccc2 (*11*). However, the affinity of the human partner protein of MNK, HAH1 (which has an electrostatic surface that is analogous to that of yeast Atx1), for the various MNK domains has recently been proposed to be essentially always the same, based on studies of the interaction between HAH1 and MNK domain pairs (*45*). Experimental data for mutations of the Cys residues of the binding loop in the human system (*45*, *46*) as well as NMR studies on the yeast system (*16*) highlight the importance of the formation of an intermediate where copper(I) bridges the two partners. Electrostatics play a role in directing partner recognition and additionally provide a non-negligible energetic contribution to the interaction; indeed, mutations designed to replace intermolecular salt bridge interactions with unfavorable contacts between side chains with the same electrostatic charge (e.g., through Lys to Glu mutations on one of the two partners) can actually abrogate protein−protein interaction (*47*). The fine details of the geometry of interaction are likely tuned by the hydrophobic contacts among residues around the metal-binding site.

There is compelling evidence for *in vivo* functional differentiation between the first four and the last two, i.e., the two closest to the membrane, metal-binding domains in ATP7A and ATP7B (*20*−*22*). The latter two domains by themselves are actually sufficient for the protein to maintain most of its biochemical properties. The close sequence similarity between the last two domains of ATP7A and those of yeast Ccc2 might be the structural basis for this physiological property. Even though the data presented here do not provide direct experimental evidence of this, it is tempting to speculate that the different dynamic properties of MNK2 in solution with respect to Ccc2 may contribute, together with its electrostatics which are suboptimal for interaction with the partner, to tuning its physiological role and, in particular, to differentiating the second from the fifth and sixth domain *in vivo*.

ACKNOWLEDGMENT

We thank Dr. Barbara Levinson for providing us with a plasmid containing the entire ATP7A gene.

SUPPORTING INFORMATION AVAILABLE

Six tables showing the experiments that were performed, the chemical shift assignments, and the upper distance limits used in structure calculations for apo-MNK2 and copper(I)-bound MNK2. This material is available free of charge via the Internet at http://pubs.acs.org.

REFERENCES

1. Linder, M. C. (1991) in *Biochemistry of Copper*, Plenum Press, New York.

2. Vulpe, C. D., and Packman, S. (1995) Cellular copper transport, *Annu. Rev. Nutr. 15*, 293−322.
3. O'Halloran, T. V., and Culotta, V. C. (2000) Metallochaperones: An Intracellular Shuttle Service for Metal Ions, *J. Biol. Chem. 275*, 25057−25060.
4. Harrison, M. D., Jones, C. E., Solioz, M., and Dameron, C. T. (2000) Intracellular copper routing: the role of copper chaperones, *Trends Biochem. Sci. 25*, 29−32.
5. Puig, S., and Thiele, D. J. (2002) Molecular mechanisms of copper uptake and distribution, *Curr. Opin. Chem. Biol. 6*, 171−180.
6. Huffman, D. L., and O'Halloran, T. V. (2000) Energetics of Copper Trafficking Between the Atx1 Metallochaperone and the Intracellular Copper-transporter, Ccc2, *J. Biol. Chem. 275*, 18611−18614.
7. Rae, T., Schmidt, P. J., Pufahl, R. A., Culotta, V. C., and O'Halloran, T. V. (1999) Undetectable intracellular free copper: the requirement of a copper chaperone for superoxide dismutase, *Science 284*, 805−808.
8. Klomp, L. W., Lin, S. J., Yuan, D., Klausner, R. D., Culotta, V. C., and Gitlin, J. D. (1997) Identification and functional expression of HAH1, a novel human gene involved in copper homeostasis, *J. Biol. Chem. 272*, 9221−9226.
9. Pufahl, R. A., Singer, C. P., Peariso, K. L., Lin, S.-J., Schmidt, P. J., Fahrni, C. J., Cizewski Culotta, V., Penner-Hahn, J. E., and O'Halloran, T. V. (1997) Metal ion chaperone function of the soluble Cu(I) receptor Atx1, *Science 278*, 853−856.
10. Petris, M. J., Mercer, J. F., Culvenor, J. G., Lockhart, P., and Camakaris, J. (1996) Ligand-regulated transport of the Menkes copper P-type ATPase efflux pump from the Golgi apparatus to the plasma membrane: a novel mechanism of regulated trafficking, *EMBO J. 15*, 6084−6095.
11. Arnesano, F., Banci, L., Bertini, I., Ciofi-Baffoni, S., Molteni, E., Huffman, D. L., and O'Halloran, T. V. (2002) Metallochaperones and metal transporting ATPases: a comparative analysis of sequences and structures, *Genome Res. 12*, 255−271.
12. Bull, P. C., and Cox, D. W. (1994) Wilson disease and Menkes disease: new handles on heavy-metal transport, *Trends Genet. 10*, 246−252.
13. Rosenzweig, A. C. (2001) Copper delivery by metallochaperone proteins, *Acc. Chem. Res. 34*, 119−128.
14. Banci, L., and Rosato, A. (2003) Structural genomics of proteins involved in copper homeostasis, *Acc. Chem. Res. 36*, 215−221.
15. Banci, L., Bertini, I., Ciofi-Baffoni, S., Del Conte, R., and Gonnelli, L. (2003) Understanding copper trafficking in bacteria: interaction between the copper transport protein CopZ and the N-terminal domain of the copper ATPase CopA from *Bacillus subtilis*, *Biochemistry 42*, 1939−1949.
16. Arnesano, F., Banci, L., Bertini, I., Cantini, F., Ciofi-Baffoni, S., Huffman, D. L., and O'Halloran, T. V. (2001) Characterization of the binding interface between the copper chaperone Atx1 and the first cytosolic domain of Ccc2 ATPase, *J. Biol. Chem. 276*, 41365−41376.
17. Wernimont, A. K., Huffman, D. L., Lamb, A. L., O'Halloran, T. V., and Rosenzweig, A. C. (2000) Structural basis for copper transfer by the metallochaperone for the Menkes/Wilson disease proteins, *Nat. Struct. Biol. 7*, 766−771.
18. Gitschier, J., Moffat, B., Reilly, D., Wood, W. I., and Fairbrother, W. J. (1998) Solution structure of the fourth metal-binding domain from the Menkes copper-transporting ATPase, *Nat. Struct. Biol. 5*, 47−54.
19. Jones, C. E., Daly, N. L., Cobine, P. A., Craik, D. J., and Dameron, C. T. (2003) Structure and metal binding studies of the second copper binding domain of the Menkes ATPase, *J. Struct. Biol. 143*, 209−218.
20. Goodyer, I. D., Jones, E. E., Monaco, A. P., and Francis, M. J. (1999) Characterization of the Menkes protein copper-binding domains and their role in copper-induced protein relocalization, *Hum. Mol. Genet. 8*, 1473−1478.
21. Voskoboinik, I., Strausak, D., Greenough, M., Brooks, H., Petris, M., Smith, S., Mercer, J. F., and Camakaris, J. (1999) Functional analysis of the N-terminal CXXC metal-binding motifs in the human menkes copper-transporting P-type ATPase expressed in cultured mammalian cells, *J. Biol. Chem. 274*, 22008−22012.
22. Huster, D., and Lutsenko, S. (2003) The distinct roles of the N-terminal copper-binding sites in regulation of catalytic activity of the Wilson's disease protein, *J. Biol. Chem. 278*, 32212−32218.
23. Eccles, C., Güntert, P., Billeter, M., and Wüthrich, K. (1991) Efficient analysis of protein 2D NMR spectra using the software package EASY, *J. Biomol. NMR 1*, 111−130.
24. Güntert, P., Braun, W., and Wüthrich, K. (1991) Efficient computation of three-dimensional protein structures in solution from nuclear magnetic resonance data using the program DIANA and the supporting programs CALIBA, HABAS and GLOMSA, *J. Mol. Biol. 217*, 517−530.
25. Archer, S. J., Ikura, M., Torchia, D. A., and Bax, A. (1991) An alternative 3D NMR technique for correlation backbone ^{15}N with side chain Hβ resonances in larger proteins, *J. Magn. Reson. 95*, 636−641.
26. Vuister, G. W., and Bax, A. (1993) Quantitative J Correlation: A New Approach for Measuring Homonuclear Three-Bond J($H^N H^\alpha$) Coupling Constants in ^{15}N Enriched Proteins, *J. Am. Chem. Soc. 115*, 7772−7777.
27. Gagné, R. R., Tsuda, S., Li, M. X., Chandra, M., Smillie, L. B., and Sykes, B. D. (1994) Quantification of the calcium-induced secondary structural changes in the regulatory domain of troponin-C, *Protein Sci. 3*, 1961−1974.
28. Wishart, D. S., and Sykes, B. D. (1994) The ^{13}C chemical shift index: a simple method for the identification of protein secondary structure using ^{13}C chemical shift data, *J. Biomol. NMR 4*, 171−180.
29. Güntert, P., Mumenthaler, C., and Wüthrich, K. (1997) Torsion Angle Dynamics for NMR Structure Calculation with the new program DYANA, *J. Mol. Biol. 273*, 283−298.
30. Herrmann, T., Güntert, P., and Wüthrich, K. (2002) Protein NMR structure determination with automated NOE assignment using the new software CANDID and the torsion angle dynamics algorithm DYANA, *J. Mol. Biol. 319*, 209−227.
31. Banci, L., Bertini, I., Ciofi-Baffoni, S., Huffman, D. L., and O'Halloran, T. V. (2001) Solution structure of the yeast copper transporter domain Ccc2a in the apo and Cu(I)-loaded states, *J. Biol. Chem. 276*, 8415−8426.
32. Case, D. A., Pearlman, D. A., Caldwell, J. W., Cheatham, T. E., Ross, W. S., Simmerling, C. L., Darden, T. A., Merz, K. M., Stanton, R. V., Cheng, A. L., Vincent, J. J., Crowley, M., Tsui, V., Radmer, R. J., Duan, Y., Pitera, J., Massova, I., Seibel, G. L., Singh, U. C., Weiner, P. K., and Kollman, P. A. (1999) *AMBER 6*, University of California, San Francisco.
33. Banci, L., Benedetto, M., Bertini, I., Del Conte, R., Piccioli, M., and Viezzoli, M. S. (1998) Solution structure of reduced monomeric Q133M2 Copper, Zinc Superoxide Dismutase. Why is SOD a dimeric enzyme? *Biochemistry 37*, 11780−11791.
34. Laskowski, R. A., MacArthur, M. W., Moss, D. S., and Thornton, J. M. (1993) PROCHECK: a program to check the stereochemical quality of protein structures, *J. Appl. Crystallogr. 26*, 283−291.
35. Laskowski, R. A., Rullmann, J. A. C., MacArthur, M. W., Kaptein, R., and Thornton, J. M. (1996) AQUA and PROCHECK-NMR: Programs for checking the quality of protein structures solved by NMR, *J. Biomol. NMR 8*, 477−486.
36. Kay, L. E., Nicholson, L. K., Delaglio, F., Bax, A., and Torchia, D. A. (1992) Pulse sequences for removal of the effects of cross correlation between dipolar and chemical-shift anisotropy relaxation mechanisms on the measurement of heteronuclear T_1 and T_2 values in proteins, *J. Magn. Reson. 97*, 359−375.
37. Grzesiek, S., and Bax, A. (1993) The importance of not saturating H_2O in protein NMR. Application to sensitivity enhancement and NOE measurements, *J. Am. Chem. Soc. 115*, 12593−12594.
38. Marquardt, D. W. (1963) An algorithm for least-squares estimation of nonlinear parameters, *J. Soc. Ind. Appl. Math. 11*, 431−441.
39. Mandel, M. A., Akke, M., and Palmer, A. G., III (1995) Backbone dynamics of *Escherichia coli* ribonuclease HI: correlations with structure and function in an active enzyme, *J. Mol. Biol. 246*, 144−163.
40. Cavanagh, J., Fairbrother, W. J., Palmer, A. G., III, and Skelton, N. J. (1996) in *Protein NMR Spectroscopy. Principles and practice*, Academic Press, San Diego.
41. Ishima, R., and Torchia, D. A. (2000) Protein dynamics from NMR, *Nat. Struct. Biol. 7*, 740−743.
42. Arnesano, F., Banci, L., Bertini, I., Huffman, D. L., and O'Halloran, T. V. (2001) Solution Structure of the Cu(I) and Apo forms of the Yeast Metallochaperone, Atx1, *Biochemistry 40*, 1528−1539.
43. Banci, L., Bertini, I., Ciofi-Baffoni, S., Gonnelli, L., and Su, X. C. (2003) A core mutation affecting the folding properties of a soluble domain of the ATPase protein CopA from *Bacillus subtilis*, *J. Mol. Biol. 331*, 473−484.
44. Banci, L., Bertini, I., and Del Conte, R. (2003) The solution structure of apo CopZ from *Bacillus subtilis*: a further analysis of the changes associated with the presence of copper, *Biochemistry 42*, 13422−13428.

45. Strausak, D., Howie, M. K., Firth, S. D., Schlicksupp, A., Pipkorn, R., Multhaup, G., and Mercer, J. F. (2003) Kinetic analysis of the interaction of the copper chaperone Atox1 with the metal binding sites of the Menkes protein, *J. Biol. Chem. 278*, 20821−20827.
46. Larin, D., Mekios, C., Das, K., Ross, B., Yang, A. S., and Gilliam, C. T. (1999) Characterization of the Interaction between the Wilson and Menkes Disease Proteins and the Cytoplasmic Copper Chaperone, HAH1p, *J. Biol. Chem. 274*, 28497−28504.
47. Portnoy, M. E., Rosenzweig, A. C., Rae, T., Huffman, D. L., O'Halloran, T. V., and Cizewski Culotta, V. (1999) Structure−function analyses of the ATX1 metallochaperone, *J. Biol. Chem. 274*, 15041−15045.
48. Koradi, R., Billeter, M., and Wüthrich, K. (1996) MOLMOL: a program for display and analysis of macromolecular structure, *J. Mol. Graphics 14*, 51−55.

BI036042S